THE ASTROPHYSICAL JOURNAL, 332:1030–1048, 1988 September 15

KINEMATICS OF THE H II REGION SHARPLESS 142. III. MOLECULAR LINE OBSERVATIONS AND ANALYSIS OF THE *IRAS* DATA

GILLES JONCAS
Observatoire de Marseille; and Département de Physique, Université Laval, and Observatoire du mont Mégantic

AND

C. KÖMPE AND J. DE LA NOË
Observatoire de Bordeaux

Received 1987 June 6; accepted 1988 March 11

ABSTRACT

The molecular cloud associated with the H II region S142 has been mapped (4'.4 resolution) in the $J = 1$–0 transition lines of ^{12}CO and ^{13}CO using the 2.5 m antenna of the Observatoire de Bordeaux. The ^{12}CO emission has an extent of 30 pc × 7 pc and has the same orientation as the optical nebula. The molecular cloud has two components separated by 25 projected parsecs; its total mass is $\sim 5600\ M_\odot$.

High-resolution observations (33″ and 20″) in the same transition lines have been carried out toward two bright rims using the 20 m antenna of the Onsala Space Observatory (Sweden) and the IRAM 30 m antenna on the Pico Veleta (Spain). These observations reveal the presence of condensations in the molecular cloud. They also suggest the presence of hot and dense gas at the position of the bright rims which can be interpreted as a dense gas layer swept up by a shock wave preceding the ionization front. Results of thermal balance calculations are consistent with the scheme that the inner molecular cloud is cooled by the ^{12}CO line emission and heated by cosmic rays.

An analysis of the infrared data gathered by *IRAS* is also presented. The IR thermal continuum emission has a larger extent at 100 μm than at 12 μm. The near-IR emission is coextensive with the ionized gas, while the far-IR emission does not follow the contours of the molecular cloud. The mean dust color temperature is 169 K for the hot, small grains and 34 K for the colder, larger grains. The amount of dust grains falls off rapidly (power law) away from its peak position. The total dust mass is $\sim 60\ M_\odot$. The total IR flux is $8.5 \pm 0.8 \times 10^{-10}$ W m^{-2}.

Bringing together all our observations of S142 we derive a gas-to-dust ratio of ~ 200 for this gas complex (excluding the cold dust missed by the *IRAS* bands). Using a power-law function for the initial mass function and published work on the stellar cluster associated with S142, we obtain a mass of 1000 $M_\odot$ for the star cluster. The star formation efficiency for the S142 gas complex was $\sim 8\%$.

Subject headings: interstellar: grains — interstellar: molecules — nebulae: H II regions — nebulae: individual (Sharpless 142) — nebulae: internal motions

I. INTRODUCTION

Multispectral analysis of young star-gas complexes is necessary in order to comprehend the interaction between the different components and the forces at play. This is why a thorough study of the S142 gas complex was initiated as part of a long-running project to study star birthplaces at different stages of their evolution.

This paper is the third of a series dealing with S142. In Paper I (Joncas and Roy 1984) a detailed study of the Hα velocity field of the ionized gas was presented showing the presence of a large-scale velocity gradient. In Paper II (Joncas *et al.* 1985) were shown the results of 21 cm aperture synthesis observations of the continuum and H I line emission. A model for S142 itself and its atomic environment was proposed. We present here millimeter wave observations of the molecular gas associated with S142 and an analysis of the infrared data of this part of the sky obtained by the *Infrared Astronomical Satellite* (*IRAS*).

Israel (1980) studied the molecular cloud associated with S142. However, his work was done within the framework of a multiobject survey. We felt that higher resolution observations were needed to adequately complement the data already gathered. In addition Israel deduced from his results that the molecular cloud was of very low mass and low density. The latter was at odds with the presence of a well-developed and continuing velocity gradient in the ionized gas. A minimum pressure discontinuity between the neutral and ionized gas is necessary to maintain the flow. A complete background on S142 was given in Papers I and II and will not be repeated here. S142 is a large (~ 35 pc) H II region located in the Perseus arm at 3.5 kpc from the Sun (Paper I). It contains the open star cluster NGC 7380 which is 2–3 × 10^6 yr old (Moffat 1971). The principal ionizing star is the spectroscopic binary HD 215835; both components are O6 stars. The mean $V_{\rm LSR}$ of the ionized gas is -35.6 ± 0.1 km s^{-1}. S142 is a relatively old object.

II. EXPERIMENTAL SET-UP AND OBSERVATIONS

a) Bordeaux Observations

The molecular cloud associated with the H II region S142 was mapped in the $J = 1$–0 lines of ^{12}CO and ^{13}CO using the Observatoire de Bordeaux 2.5 m antenna. An attempt was made to detect the $J = 1$–0 C^{18}O line. The ^{12}CO observations were carried out in 1985 February, the ^{13}CO observations in 1984 February and March, and 1985 March. Table 1 shows the data characteristics, each column being self-explanatory. A complete description of the equipment can be found in Baudry *et al.* (1981).

The spectral line observations were obtained by frequency switching the receiver. The calibration was made against the sky brightness temperature and a controlled temperature load. The spectra are given in units of $T_A{}^*$ (Kutner and Ulich 1981). The values $T_A{}^*$ and $T_R{}^*$ are related by $T_R{}^* = T_A{}^*/\eta_{\rm fss}$; the forward spillover and scattering efficiency ($\eta_{\rm fss}$) was measured to be 0.9. Several times during an observing period a reference source was observed to check the stability of the system from day to day and month to month. No significant drifts were found. The S142 molecular cloud was mapped using a 4′ spacing. Each location on the molecular cloud was observed long enough to obtain a noise level (1 σ) of 0.15 K for ^{12}CO, 0.08 K for ^{13}CO, and 0.1 K for C^{18}O. No C^{18}O line was detected in the cloud's core. The typical system temperature was about 1000 K at ^{13}CO and 1600 K at ^{12}CO.

b) Onsala and Pico Veleta Observations

High spatial resolution observations have been carried out in the $J = 1$–0 lines of the ^{12}CO, ^{13}CO, and C^{18}O molecules at the Onsala Space Observatory (OSO) 20 m millimeter wave antenna in 1986 June. Additional ^{13}CO spectra had been gathered previously in 1986 January with the IRAM 30 m telescope located on the Pico Veleta.

The purpose of these observations was the study of two bright rims visible optically called BN and BS (see Fig. 3*a* in Paper I). The spectra are located on two strips ($\sim 5'$ long), each strip crossing one of the bright rims in the east-west direction. The spacing of the spectra was about one HPBW (see Table 1). The reference point for BN is at $22^{\rm h}46^{\rm m}12^{\rm s}$, 57°49′, while the reference point for BS is at $22^{\rm h}45^{\rm m}50^{\rm s}$, 57°47′. All coordinates are for 1950. These points coincide with the positions of the bright rims. These observations will also give some insights on the fine structure of the molecular cloud.

The spectra have been obtained by frequency switching. No receiver stability and no pointing checks have been done at OSO. On Pico Veleta pointing has been checked on the SiO maser R Cas. No significant errors were found. The system temperature at OSO was about 500 K and at IRAM about 800 K. Each OSO spectrum has an rms noise (1 σ) of 0.2 K for ^{12}CO, 0.07 K for ^{13}CO, and 0.06 K for C^{18}O. The IRAM data have an rms noise of 0.16 K.

III. ANALYSIS OF THE MOLECULAR LINE OBSERVATIONS

a) The Bordeaux Observations

i) *Description of the Data*

Figures 1*a* and 1*b* display maps of the individual ^{12}CO and ^{13}CO spectra. The reference point (0, 0) corresponds to the phase center ($22^{\rm h}46^{\rm m}00^{\rm s}$, 57°48′00″) of previously obtained 21 cm observations (Paper II). Table 2 shows the spectra characteristics. Columns (1) and (2) give the offset positions of the observed lines in arcminutes, columns (3) and (6) give the antenna temperatures ($T_A{}^*$) for both isotopes, columns (4) and (7) give the LSR velocities, and columns (5) and (8) give the FWHM. At three positions in the molecular cloud [(4, 4), (0, 0), (0, −4)] the ^{12}CO spectra are best-fitted by a double component Gaussian. The mean separation is 2 km s^{-1}. There are no double-peaked ^{13}CO lines, but the ^{13}CO profiles at positions (0, 0) and (0, −4) have large FWHM. The mean LSR velocity of the cloud is -39.3 ± 2.3 (1 σ) km s^{-1} in ^{12}CO and -39.4 ± 1.9 (1 σ) km s^{-1} in ^{13}CO. The mean ^{13}CO and ^{12}CO FWHM are 2.0 ± 0.5 (1 σ) km s^{-1} and 2.2 ± 0.6 (1 σ) km s^{-1}, respectively.

Figures 2*a* and 2*b* show the integrated intensity maps for the ^{12}CO and ^{13}CO observations. The LSR velocity range is −45 to −35 km s^{-1}. The S142 molecular cloud is not a big object, being roughly 30 pcs × 7 pcs in extent (FWHM). The cloud is oriented along a NE–SW axis thus following the same inclination as the optical nebula (Paper II). The ^{12}CO emission is somewhat more extended than the ^{13}CO emission but by only two beamwidths in both right ascension and declination. The S142 molecular cloud has two components. The northeastern (NE) component has an extended core in ^{13}CO and the emission falls off more sharply on its western side. Its peak emission is located one beamwidth to the north of the 21 cm radio continuum peak when we compare maps of equal resolution. The southwestern (SW) component has the same peak antenna temperature as the other component. The NE and SW components are attached to each other at the 3 σ level in the ^{12}CO integrated intensity map only. However, both components are connected at the 3 σ level in the $T_A{}^*$ ^{13}CO contour map (see Fig. 10). The SW component is redshifted by 4 km s^{-1} with respect to the NE component. The velocity difference appears sharply in both lines; however the ^{12}CO line has an extended red wing at position (−4, −4).

ii) *Derivation of the Physical Parameters*

As a first step we derive the H$_2$ column density ($N_{\rm H_2}$) using the LTE derivations from Dickman (1978*a*). To use the LTE calculations both ^{12}CO and ^{13}CO lines must be observed at the same location where the following assumptions are made: (1) the molecules along the line of sight possess a uniform excitation temperature ($T_{\rm EX}$) and density, (2) both isotopes have the same $T_{\rm EX}$, (3) ^{12}CO is thermalized (i.e., $T_{\rm EX}$ is equal to the kinetic temperature (T_K)), (4) the emission fills the beam, and (5) ^{12}CO is optically thick. The ^{13}CO column density ($N_{\rm ^{13}CO}$) is then given by

$$N_{\rm ^{13}CO} = \frac{2.31 \times 10^{14} \tau_{\rm ^{13}CO} \Delta V_{\rm ^{13}CO} (T_K + 0.91)}{1 - \exp(-5.29/T_K)} ,$$

where $\tau_{\rm ^{13}CO}$ is the line opacity and $\Delta V_{\rm ^{13}CO}$ is the FWHM of the ^{13}CO line. The results of these calculations are given in column

TABLE 1

MOLECULAR DATA CHARACTERISTICS

TRANSITION LINE	ν (GHz)	BORDEAUX 2.5 m ANTENNA		OSO 20 m ANTENNA		IRAM 30 m ANTENNA	
		HPBW	Channel width (km s^{-1})	HPBW	Channel width (km s^{-1})	HPBW	Channel width (km s^{-1})
^{12}CO ($J = 1$–0)	115.271	4′3	0.26	33″	0.65		
^{13}CO ($J = 1$–0)	110.201	4.4	0.27	34	0.68	22″	0.27

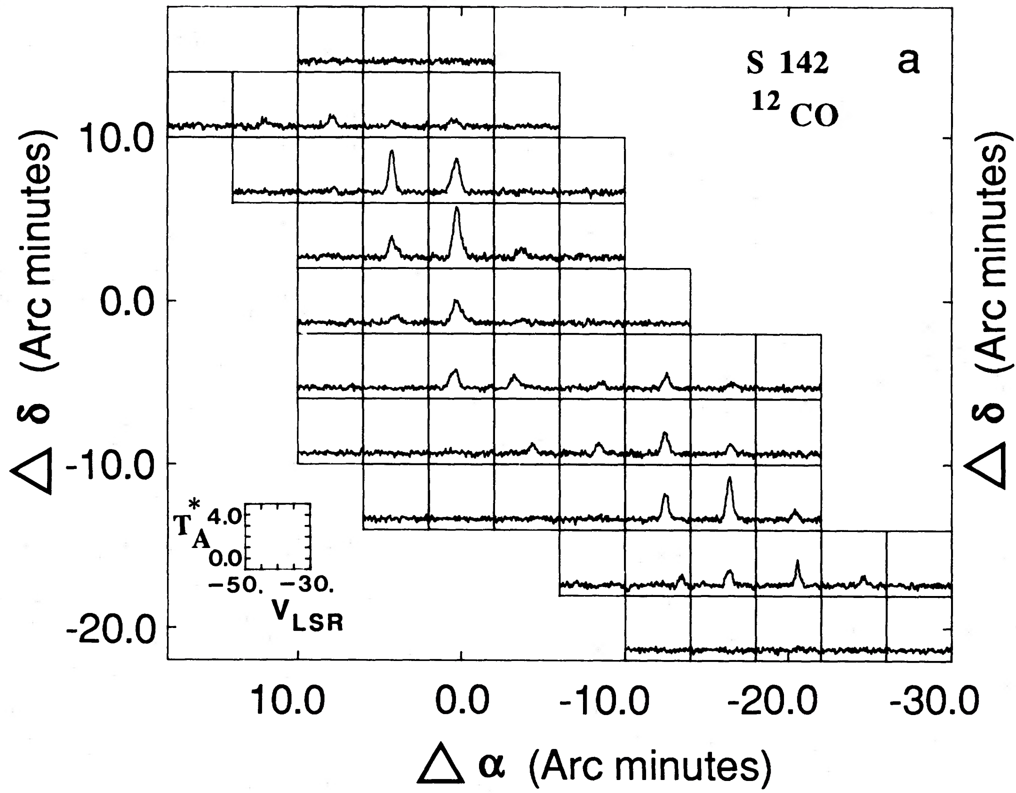

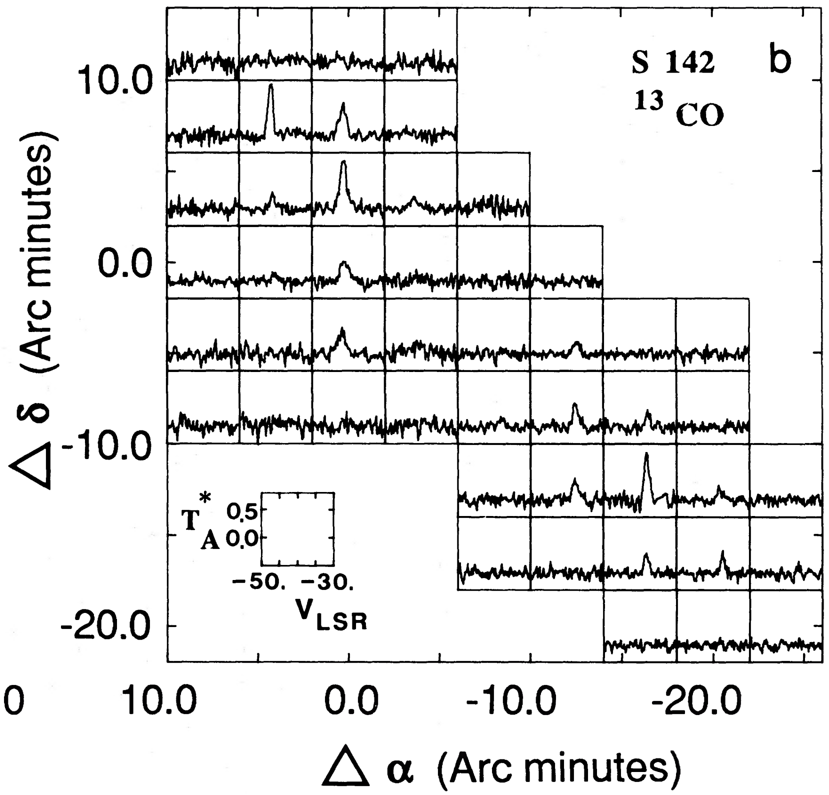

FIG. 1*a*.—The ^{12}CO spectral lines observed in S142 with the Bordeaux antenna. The 1950 coordinates of the reference point are 22^h46^m and 57°48′. The velocity and antenna temperature scales are identical for all the spectra; they are plotted in the lower left corner.

FIG. 1*b*.—The ^{13}CO spectral lines observed in S142 with the Bordeaux antenna. The coordinates of the reference point are the same as in Fig. 1*a*. The velocity and antenna temperature scales are identical for all the spectra; they are plotted in the lower left corner.

TABLE 2

Molecular Spectral Line Data: Bordeaux Observations

Offsets		^{12}CO			^{13}CO			
Δα	Δδ	T_A^* K	$V_{\rm LSR}$ km s^{-1}	FWHM km s^{-1}	T_A^* K	$V_{\rm LSR}$ km s^{-1}	FWHM km s^{-1}	$N_{^{13}\rm CO}$ 10^{15} cm^{-2}
12′............	12′	0.53	−40.1	2.7				
8............	12	0.97	−39.47	2.3				
4............	12	0.47	−40.9	2.1				
0............	12	0.58	−42.3	3.0				
8............	8	0.48	−38.8	1.4				
4............	8	3.9	−41.2	1.91	0.98	−41.37	1.52	2.2
0............	8	2.95	−41.54	2.81	0.53	−41.44	2.3	1.8
4............	4	{1.86	−41.20	1.9	0.27	−40.82	1.4	0.6
		0.68	−39.2	1.4				
0............	4	4.44	−41.20	2.61	0.85	−41.27	2.2	2.8
−4............	4	0.8	−41.5	2.9	0.18	−41.8	2.9	1.2
0............	0	{1.84	−41.52	2.76				
		0.46	−39.0	4	0.36	−41.0	2.8	1.6
0............	−4	{1.13	−43.0	2.0				
		1.41	−41.4	1.6	0.35	−41.8	2.4	2.0
−4............	−4	0.99	−43.82	2.4				
−8............	−4	0.5	−37.1	2.4				
−12............	−4	1.25	−37.29	2.1	0.22	−37.3	2.1	0.8
−16............	−4	0.41	−37.0	3.0				
−4............	−8	0.84	−38.3	2.1				
−8............	−8	0.95	−37.86	2.1				
−12............	−8	1.93	−37.69	2.3	0.42	−37.66	1.7	1.1
−16............	−8	0.9	−37.68	2.2	0.26	−37.8	1.3	0.8
−12............	−12	2.4	−37.62	2.07	0.32	−37.7	2.0	0.9
−16............	−12	3.87	−38.00	2.06	0.84	−38.09	1.6	2.1
−20............	−12	0.77	−37.91	2.0	0.17	−38.0	2.2	0.9
−12............	−16	0.85	−32.8	1.6				
−16............	−16	1.39	−38.14	2.2	0.34	−38.17	1.6	0.9
−20............	−16	2.00	−37.17	1.50	0.36	−37.32	1.2	0.7
−24............	−16	0.79	−37.1	1.8				

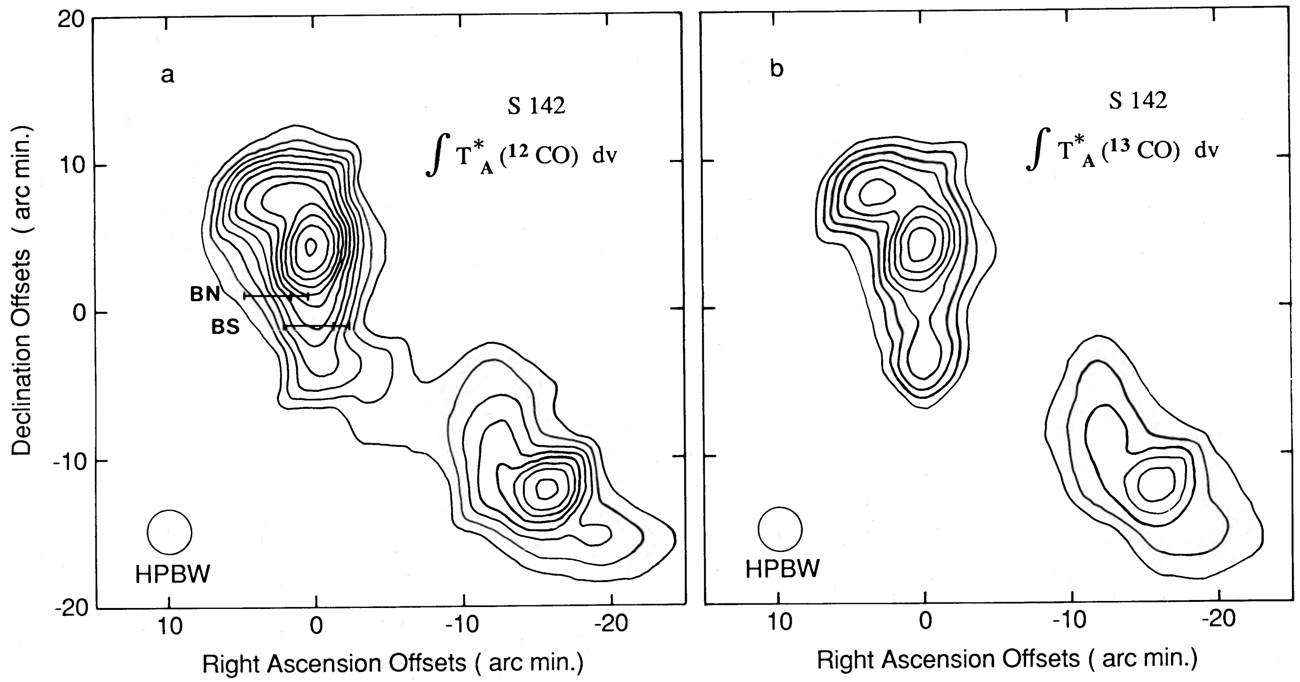

Fig. 2*a*.—Integrated intensity map of the ^{12}CO (J = 1–0) emission line of the S142 cloud. The angular resolution is 4.′3, shown in the lower left corner. The mapping was done in steps of 4′. The lowest contour is 1.5 K km s^{-1}, and the contour interval is 1.0 K km s^{-1}. The coordinates of the reference point are the same as in Fig. 1. The strips along which high spatial resolution were secured are identified.

Fig. 2*b*.—Integrated intensity map of the ^{13}CO (J = 1–0) emission line of the S142 cloud. The angular resolution is 4.′4, shown in the lower left corner. The mapping was done in steps of 4′. The lowest contour is 0.25 K km s^{-1}, and the contour interval is 0.25 K km s^{-1}. The 1950 coordinates of the reference point are the same as in Fig. 1.

[illegible] of Table 2. Using a $N_{H_2}/N_{^{13}CO}$ ratio of $(5 \pm 2.5) \times 10^5$ (Dickman 1978*a*) and assuming the NE component to be a sphere having a diameter of 9 pc, we get for the core a mean H_2 density (n_{H_2}) of ~ 50 cm^{-3}. Calculations of the minimum H_2 density necessary to thermalize ^{12}CO indicate that n_{H_2} must lie in the range 100–1000 cm^{-3}. Thus either the molecular cloud is flatter along the line of sight or at least one of the previous assumptions is not fulfilled. The ^{12}CO emission is optically thick since the ratio of the integrated intensity of the ^{12}CO and ^{13}CO lines has a mean value of 6 far from the terrestrial abundance ratio of 89 and under such conditions ^{12}CO is probably thermalized. So we may err in assuming that conditions 1, 2, and 4 are respected by the S142 molecular cloud.

To determine the mass (M) of the molecular cloud we use (Dickman 1978*b*)

$$M = (\alpha D)^2 \frac{N_{H_2}}{A_V} \mu m_H \sum_i A_{V_i} \quad g .$$

From Bohlin, Savage, and Drake (1978) we know that $N_{H_2} = 0.94 \times 10^{21} A_V$, μ is the molecular weight, and taking into account the presence of helium we have $\mu = 2.77$ amu, α is the HPBW in radians, D is the distance to the cloud in centimeters, and i refers to each offset position. In order to relate the mass to the ^{13}CO column density, we use $A_V = 4 \times 10^{-16} N_{^{13}CO}$ (Dickman 1978*a*). We thus obtain a low value for the cloud mass; our calculations yield a value of 3.5×10^3 $M_\odot$ for the total mass of the molecular cloud—70% of this mass is concentrated in the NE component.

In large-scale galactic structure studies of molecular clouds the following relation (Bloemen *et al.* 1986) is used to derive the cloud mass:

$$\frac{N_{H_2}}{\int T_A^*(^{12}CO)dv} = 2.8 \pm 0.4 \times 10^{20} .$$

Applying it to the Bordeaux observations a high value of 7.8×10^3 $M_\odot$ is obtained for the mass of the molecular cloud.

b) The Onsala and Pico Veleta Observations

i) *Description of the Data*

The ^{13}CO observations toward BN have been carried out using the OSO and IRAM antennas. The spectra of both observations have the same reference point and follow the same direction (see Fig. 2*a*). Figure 3*a* shows the IRAM spectra, and Figures 3*b* and 3*c* show the OSO spectra. Tables 3A and 3B show the spectra characteristics; the information is the same as in Table 2. Both sets of spectra display the same behavior: the highest intensity is at the reference point and the intensity distribution is asymmetric about this point, dropping faster on the west side. Four Pico Veleta spectra show two line components. These two components are found in only one of the OSO spectra, at $\Delta\alpha = -32$. The velocity of the main component is -40 km s^{-1}; the other component changes from -36.8 to -38.2 km s^{-1} as one moves from west to east.

The BN ^{12}CO and $C^{18}O$ observations have all been carried out with the OSO telescope. The ^{12}CO intensity distribution is similar to the ^{13}CO distribution, and line splitting is present at roughly the same velocities but at different locations. $C^{18}O$ was not detected.

All observations toward BS have been obtained at OSO. The spectra are displayed in Figure 4 and their characteristics are listed in Table 3C. These spectra show a similar asymmetric intensity distribution about the reference point as for BN. Line splitting occurred at only one position ($\Delta\alpha = -32$) and one molecule, ^{12}CO. $C^{18}O$ was detected only at the reference position with a line intensity of 0.24 K at -41.8 km s^{-1}.

ii) *Analysis of the Physical Parameters*

The following observational evidences tend to prove that the S142 molecular cloud is made up of condensations smaller than the beam of the Bordeaux antenna: (1) the high-resolution observations were all taken inside position (0, 0) of the Bordeaux mapping where $T_A^* = 1.8$ K; (2) in both strips large variations in antenna temperatures were observed (e.g., 0.5–8.3 K in ^{12}CO for BS); (3) if we compare OSO and IRAM data taken at the same position (the reference point in BN), the IRAM antenna temperature is more than twice as large; (4) there is a ^{12}CO velocity gradient going from east to west in the BN strip while there is no obvious one in BS, indicating variations in ^{12}CO opacity. The opposite is true for the ^{13}CO line, indicating the presence of a complicated velocity field. These observations even indicate the presence of an inhomogeneous medium inside the condensations. The observed line splitting in the ^{13}CO spectra can be explained by the presence of two condensations along the same line of sight. Another possible explanation is the gradual mingling of the molecular cloud components (NE and SW) since their mean velocities are respectively -41.4 and -37.8 km s^{-1}, close to the values for the high-resolution spectral components.

TABLE 3A

MOLECULAR SPECTRAL LINE DATA OF BN: OSO OBSERVATIONS

OFFSETS		^{12}CO			^{13}CO			
$\Delta\alpha$	$\Delta\delta$	T_A^* K	V_{LSR} km s^{-1}	FWHM km s^{-1}	T_A^* K	V_{LSR} km s^{-1}	FWHM km s^{-1}	$N_{^{13}CO}$ 10^{15} cm^{-2}
192″	0″							
160	0	0.8	−41.8	2				
128	0	0.6	−40.5	3				
96	0	1.4	−40.4	4.6	0.31	−39.8	1.0	0.6
64	0	4.2	−40.90	2.6	1.05	−40.06	1.5	2.9
32	0	4.8	−40.63	2.79	1.5	−40.03	1.47	4.5
0	0	4.9	−40.45	3.62	1.97	−39.99	1.65	6.5
					0.18	−37.5	2.1	
−32	0	1.1	−39.9	4.4	0.52	−39.91	1.0	1.2
		3.6	−37.83	1.26	0.49	−37.0	1.0	1.1
−64	0	0.7	−41.5	2.7				
		1.1	−37.7	1.1				

An interesting feature has still to be explained: in the BN and BS strips, the spectrum with the highest intensity is found at the reference position which coincides with the position of the bright rims. This particular behavior is clearly seen in the BS strip (Fig. 4), where two intense spectra appear to be superposed on a more or less constant background. These intense lines are evidence for hot and dense gas adjacent to the bright rims. The extent of this gas is 0.7 pc in BN and 1.1 pc in BS (OSO observations). Note, however, that these numbers may be overestimated due to beam dilution. The BN hot gas layer appears narrower in the IRAM observations. Current theories (see, e.g., McKee and Hollenbach 1980) predict the existence of a shock wave preceding the ionization front and sweeping up a layer of hot and dense gas. We may be observing this swept-up gas.

The next step is to evaluate the mean density of the condensations observed in the molecular cloud. Using the LTE procedure described in § III*a*, we derived $N_{^{13}\mathrm{CO}}$ from the high spatial resolution data (see col. [9] of Table 3). The Onsala ^{13}CO column densities are larger than the Bordeaux ^{13}CO column densities. Since the intensity decreases to zero in the east and west direction of the BN and BS strips, we assume that our spectra cover a whole condensation in both cases. Using condensation diameters of 2'.3 (7×10^{18} cm) for BN and 4'.3 (14×10^{18} cm) for BS and assuming the position of highest $T_A{}^*$ to be the center of a condensation, we derive the volume density of H$_2$ (n_{H_2}) to be 930 cm^{-3} for BN and 760 cm^{-3} for BS. The densities are high enough to thermalize the carbon monoxide. As suggested by the IRAM observations, the high-density structures have to be studied at still higher spatial resolution.

TABLE 3B

^{13}CO SPECTRAL LINE DATA OF BN: IRAM OBSERVATIONS

OFFSETS Δα	Δδ	$T_A{}^*$ K	V_{LSR} km s^{-1}	FWHM km s^{-1}
100″.........	0″			
80	0	0.9	−40.4	1.0
60	0	calibration error		
40	0	1.4	−40.0	1.5
20	0	3.7	−39.9	1.3
		1.0	−38.2	0.4
0	0	4.4	−39.7	1.2
		0.5	−37.7	0.6
−20	0	1.2	−40.0	1.4
		0.8	−37.4	1
−40	0	0.5	−40.1	1.6
		1.6	−36.8	1.1
−60	0	0.6	−37.0	0.9
−80	0			
−100	0			

The detection of the BN and BS condensations and five high-resolution spectra toward the center of the molecular cloud (not shown in this paper) suggests a two-component cloud model: molecular condensations separated by more tenuous molecular and/or atomic gas. We can use our high-resolution observations to derive typical characteristics of these condensations. Assuming a spherical shape with a diameter of 3.5 pc, we obtain a mean kinetic temperature of 10 K, a mean mass of $\sim 300\ M_{\odot}$, and a mean density of ~ 200 cm^{-3}. The condensations found in S142 resemble those found by Blitz and Stark (1986) in the Rosette molecular cloud. In fact more and more observational evidence shows that molecular clouds are made up of condensations (see, e.g., Kahane, Guilloteau, and Lucas 1985, and especially in Perault, Falgarone, and Puget 1985). The sizes of the S142 condensations are about 3 times those found by Martin-Pintado *et al.* (1985) who detected structures ranging in size from <0.2 pc to >1.4 pc in several objects. The physical condition of the tenuous gas is still debated: either it is cold gas produced by the evaporation of the condensation or the gas is hot and sufficient pressure exists to keep the condensations in equilibrium.

To summarize, the S142 molecular cloud is a relatively small cloud and is made up of two components. High spatial resolution observations indicate that the molecular cloud is made up of high-density condensations. The velocity field inside the molecular cloud seems fairly complicated. Its mass is between 3500 $M_{\odot}$ and 7800 $M_{\odot}$.

IV. ANALYSIS OF THE *IRAS* DATA

a) *The Data*

The *IRAS* mission, instruments, data reduction, and calibration procedures are described in the *IRAS Explanatory Supplement* (1985). The observations were carried out simultaneously at 12, 25, 60, and 100 μm with 4′–6′ spatial resolution. The absolute calibration is accurate to 5% at 12, 25, 60 μm and to 10% at 100 μm. However the passage over a bright IR

TABLE 3C

MOLECULAR SPECTRAL LINE DATA OF BS: OSO OBSERVATIONS

OFFSETS		^{12}CO			^{13}CO			
Δα	Δδ	$T_A{}^*$ K	V_{LSR} km s^{-1}	FWHM km s^{-1}	$T_A{}^*$ K	V_{LSR} km s^{-1}	FWHM km s^{-1}	$N_{^{13}\mathrm{CO}}$ 10^{15} cm^{-2}
224″............	0″	0.5	−40.7	5.2				
192	0	0.5	−44.5	1.1				
		1.5	−41.6	2.2	0.27	−40.0	1.4	0.6
160	0	2.6	−41.29	1.9	0.27	−40.0	3	1.2
128	0	2.8	−41.34	2.4	0.75	−40.29	1.5	1.9
96	0	2.0	−42.34	2.6	0.44	−41.6	1.8	1.4
64	0	3.1	−42.26	2.7	0.89	−41.45	1.6	2.2
32	0	7.3	−42.19	2.7	2.09	−41.5	1.9	7.6
0	0	8.3	−42.60	2.73	2.9	−41.7	1.7	10.7
−32	0	3.1	−42.69	2.4	0.5	−41.65	2.1	2.0
		0.5	−39.5	2.3				
−64	0	1.2	−42.6	2.6	0.22	−41.8	2.0	0.9

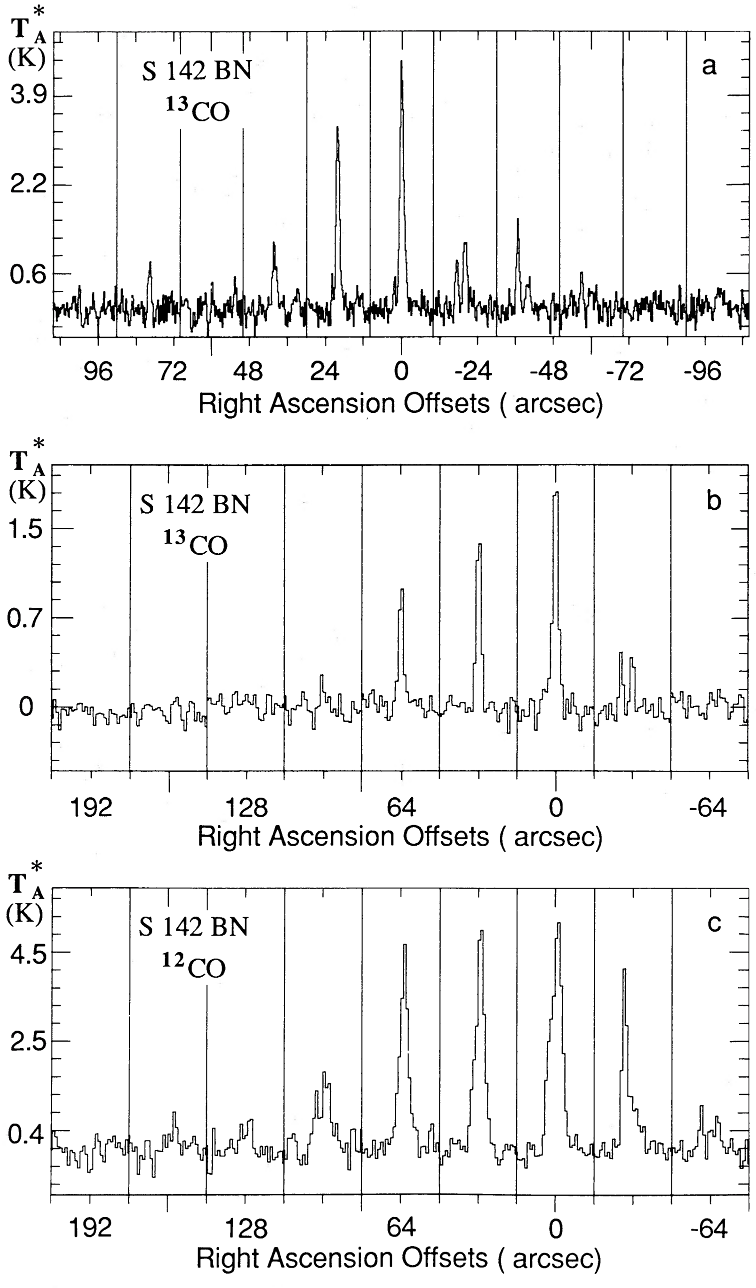

FIG. 3.—The high spatial resolution spectra observed along BN. (*a*) IRAM ^{13}CO spectra; (*b*) OSO ^{13}CO spectra, and (*c*) OSO ^{12}CO spectra. The velocity range is -30 to -50 km s^{-1} starting on the left side of the spectra.

source (e.g., the Galactic plane) can affect the photometry by as much as 70% at 100 μm due to a remanence effect. Thus the different HCON (hours confirmed) catalogs must be compared to check on this effect. The extraction of the S142 maps from the *IRAS* sky brightness images was done via AIPS (NRAO software). From these maps a locally determined background was removed. It was computed via four rectangular areas surrounding the object. The mean value of the IR intensity was chosen as the background. The variation from one area to the next was small ($\sigma < 2$ MJy sr^{-1}) except at 100 μm where $\sigma = 7$ MJy sr^{-1}. No color correction was applied to the data. No attempt was made to subtract IR point sources from the sky maps; they are not strong enough to affect them.

Figures 5*a*–*d* show the IR continuum maps of the S142 gas complex from a 60′ square field. The last contour is at the 3 σ level. At that level, S142 is about 35′ × 25′ in extent at 12 and 25 μm and 40′ × 30′ at 60 and 100 μm. The maps do not show any particular shapes except for a tendency to a sharper decrease of the emission on the east side. The emission peaks are within 4′ from the 21 cm continuum emission peak (Paper II), the 25 micron peak being the closest at 1′. Both the 12 and 25 μm maps are coextensive with the 21 cm continuum map. All maps show some similarities with the latter, the 12 μm map having the closest resemblance (compare Fig. 5*a* with Fig. 10*b*). A second peak of emission is present at wavelengths longer than 12 μm and corresponds to a sharp dark globule adjacent to the ionized filament extending north of the nebula (see POSS). Table 4 lists for each wavelength some of the character-

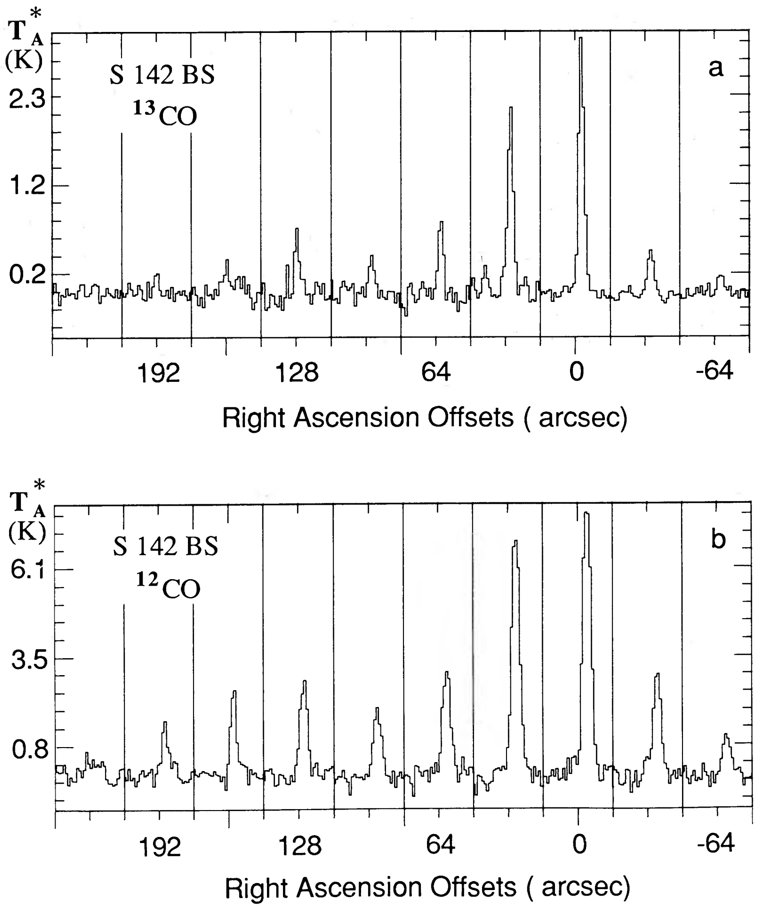

FIG. 4.—The high spatial resolution spectra observed along BS. (*a*) ^{13}CO spectra and (*b*) ^{12}CO spectra. The velocity range is -30 to -50 km s^{-1} starting on the left side of the spectra.

istics of the IR continuum emission: the value of the peak of emission, its position, the emission noise (1 σ), and the total flux emitted at the 3 σ level.

The 3 σ contour located to the southeast of S142 (Fig. 5) may be related to the H II region S143. There is some degree of spatial superposition between the radio continuum contour (Fig. 1 in Paper II) and the IR contour for all wavelengths except at 100 μm.

Table 5 lists all the *IRAS* point sources located within the 100 μm emission 3 σ boundary; objects 32 to 50 inclusively are superposed to the molecular cloud. For each object the position is given as well as the different color temperatures [the flux values come from a release prior to the latest version (2.0) of the point source catalog]. A search was made for optical or radio 21 cm counterparts to these sources. No radio counterparts were found and no IR point sources are present in the core of the molecular cloud. Ten sources have optical counterparts: three are stars from the cluster NGC 7380 (Moffat 1971), six are visible on the POSS (considering their 12 μm fluxes, three may be stars), and one corresponds to an Hα knot present in the H II region (see Fig. 2 of Paper II). Two objects are in an obscuring zone crossing S142 and one is a dark globule. Of particular interest is object 42. In a 12/25/60 μm color-color diagram, this object is located in an area defined

TABLE 4

CHARACTERISTICS OF THE IR CONTINUUM EMISSION

λ μ	PEAK FLUX M Jy sr^{-1}	PEAK POSITION α(1950)	 δ(1950)	σ M Jy sr^{-1}	TOTAL FLUX Jy
12…………	50	22^{h}45^{m}52^s	57°54′47″	0.50	439 ± 61
25…………	126	22 45 50	57 50 47	0.78	914 ± 128
60…………	547	22 45 36	57 52 57	4.37	6210 ± 869
100…………	894	22 45 51	57 52 47	11.91	13400 ± 1876

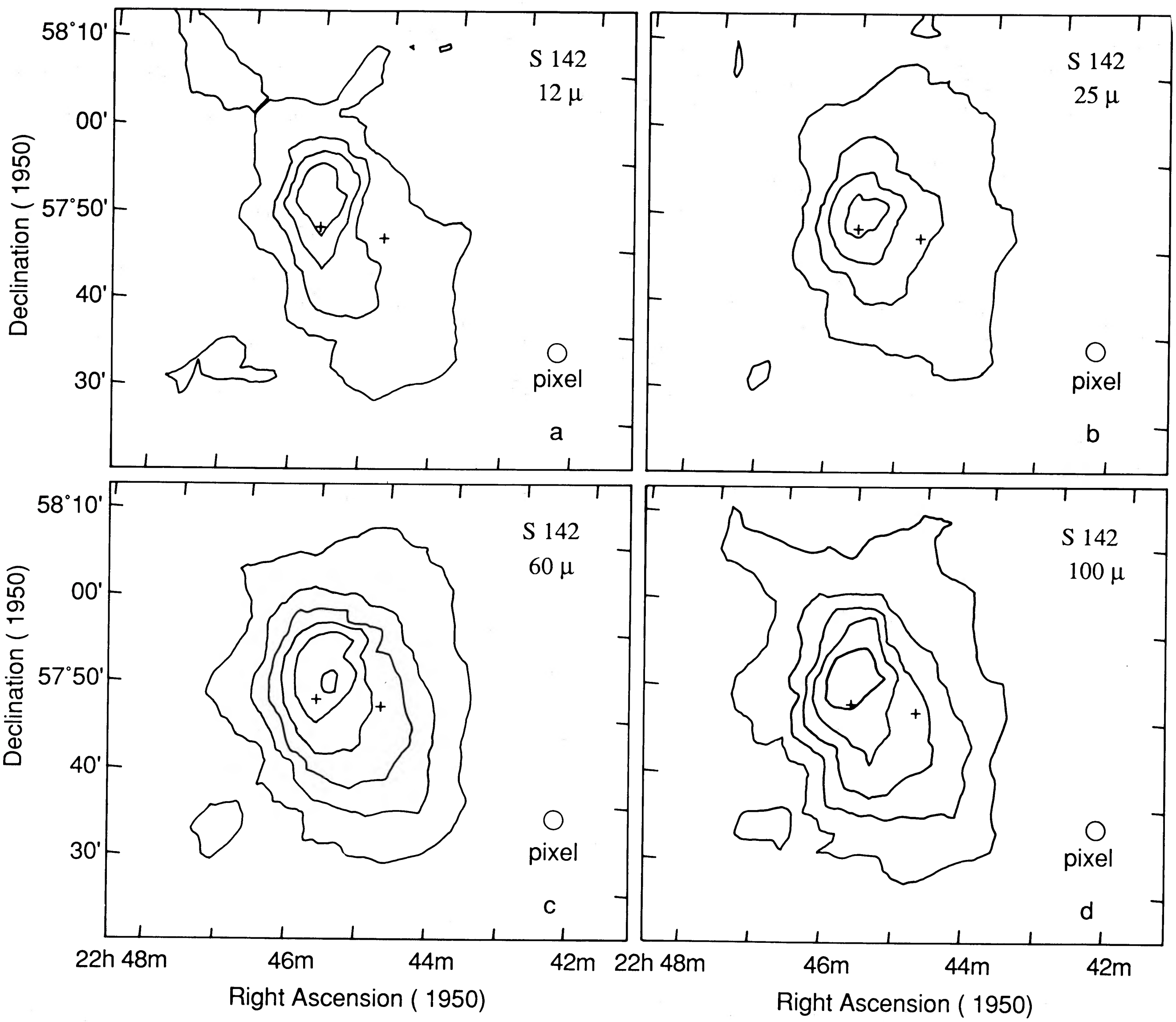

FIG. 5.—(*a*) The 12 μm map of S142. The contour levels are at 16.60, 21.95, 29.03, and 38.40 M Jy sr^{-1}. (*b*) The 25 μm map of S142. The contour levels are 31.57, 45.46, 65.46, and 94.26 M Jy sr^{-1}. (*c*) The 60 μm map of S142. The contour levels are at 36.10, 61.02, 103.1, 174.3, 294.5, and 497.7 M Jy sr^{-1}. (*d*) The 100 μm map of S142. The contour levels are at 105.5, 164.9, 257.6, 402.5, and 628.9 M Jy sr^{-1}. The pixel size is 2′. The crosses indicate the position of the main exciting stars; the easternmost star is HD 215835.

TABLE 5

IR POINT SOURCES IN S142

No.	α(1950)	δ(1950)	T_d(12/25)	T_d(25/60)	T_d(60/100)	Remarks
25............	$22^h43^m39^s.8$	57°33′20″.9	218 K	60 K	23 K	
30............	22 44 20.5	57 34 27.0	147	78	21	
32............	22 44 39.4	57 42 27.0	193	53	29	Dark globule
33............	22 44 41.6	58 01 17.9	139	62	38	POSS
34............	22 44 42.5	58 08 03.0	194	61	26	POSS
36............	22 45 03.5	57 49 33.9	118	62	45	Moffat 12
41............	22 45 22.0	57 40 03.9	190	57	24	In obscuration zone
42............	22 45 22.9	57 45 33.0	178	89	21	Probable T Tauri
43............	22 45 27.3	58 02 45.9	270	78	17	Carbon star, POSS
44............	22 45 46.2	57 51 27.9	167	55	32	Hα knot
45............	22 45 48.4	57 46 59.0	136	54	50	Moffat 24, peaks at 60 μm
46............	22 45 56.8	57 59 01.9	306	62	26	
47............	22 46 02.5	57 45 56.0	201	50	23	In obscuration zone
48............	22 46 02.6	57 41 18.7	204	53	59	POSS, peaks at 60 μm
50............	22 46 15.4	57 44 54.9	111	63	58	Moffat 7, peaks at 60 μm
53............	22 46 37.1	58 03 56.9	184	63	21	
54............	22 46 52.9	57 59 02.9	217	58	22	POSS
56............	22 47 08.7	57 37 28.9	248	64	23	POSS

only by T Tauri stars (Beichman *et al.* 1986). Baade (1983), using an extensive photographic photometry survey, also concluded the presence of T Tauri stars in the cluster NGC 7380.

b) *Derivation of the Physical Parameters*

The dust color temperatures [$T_d(12/25)$, $T_d(25/60)$, $T_d(60/100)$] were calculated using the formula given in Evans (1980)

$$T_d = \frac{hc/k(1/\lambda_2 - 1/\lambda_1)}{(3+n)\ln(\lambda_1/\lambda_2) + \ln(I_\nu(\lambda_1)/I_\nu(\lambda_2))},$$

where I_ν is the IR intensity. This expression follows from the definition of the color temperature which is approximately equal to the dust temperature when the emission is optically thin. A value of one will be used throughout for the exponent of the emissivity law ($Q \approx \lambda^{-n}$). The IR intensities were binned to a 4′ resolution around the reference point of the molecular and 21 cm observations. The temperature was calculated only if the intensities were above the 3 σ level at both wavelengths. Figures 6(*a*–*c*) show the results of these calculations. Looking at these results one must keep in mind that the dust grains may have a variety of temperatures along any line of sight either because of differences among grain types at the same location or because heating conditions vary along the line of sight. The uncertainty for the individual temperature values is 7% [$T_d(12/25)$ and $T_d(25/60)$] or 10% [$T_d(60/100)$] if we take into account only the accuracy of the absolute calibration.

The mean value of $T_d(12/25)$ is 169 K, the standard deviation is large: 21 K. An east-west temperature gradient seems to be present across the gas complex except in the south where the behavior is more chaotic. The highest dust temperature is located 6′ northeast of the 12 and 25 μm emission peaks, where the 21 cm and IR emissions show a steep gradient. The mean value of $T_d(25/60)$ is 61 K (1 σ = 2 K) and the mean value of

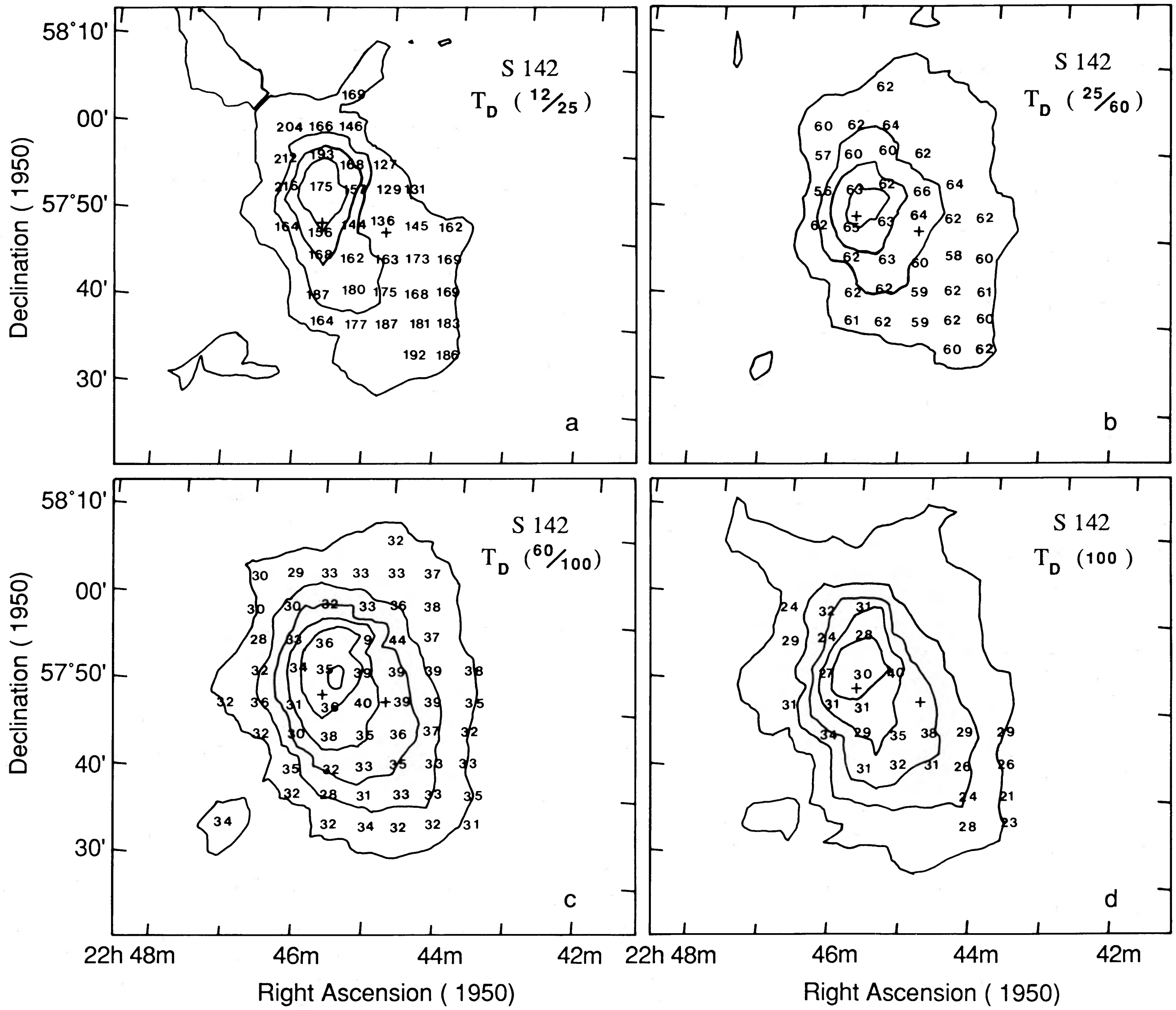

FIG. 6.—The calculated dust color temperatures are superposed to the appropriate contour maps. The data were binned to give a 4′ spatial resolution. The crosses have the same function as in Fig. 5. (*a*) $T_d(12/25)$ over the 12 μm map. (*b*) $T_d(25/60)$ over the 25 μm map. (*c*) $T_d(60/100)$ over the 60 μm map. (*d*) The dust temperature calculated from the 100 μm intensity over the 100 μm map.

$T_d(60/100)$ is 34 K (1 $\sigma = 3$ K). The highest temperatures are close to the peaks of emission and to the exciting stars. The coldest temperatures are at the northeastern end of the emission zone, near the molecular cloud's core. The relatively high value of $T_d(60/100)$ indicates that the IR continuum emission at 60 μm comes in part from hotter grains. There is a very slow decrease of the temperatures away from the peak ($r^{-0.07}$), far from the temperature distribution derived by Scoville and Kwan (1976) ($r^{-0.4}$) for a spherical nebula with a central source. This comes from the geometry of the gas complex, most of the far-IR emission being emitted from the outskirt of the nebula and the interface with the neutral gas.

In an attempt to check on the presence of colder grains, we used the relation of Hildebrand (1983),

$$I_\nu = \frac{m_{\rm H}\,\mu N_{({\rm HI}+{\rm H}_2)}\,B_\nu(T)}{C}$$

where I_ν is the infrared intensity, $m_{\rm H}$ is the mass of the hydrogen atom, μ is the molecular weight, N is the gas column density determined from our H I and CO observations, $B_\nu(T)$ is the Planck function intensity, and C represents the properties of the dust grain mixture and the dust-to-gas ratio

$$C = \frac{4a\rho}{3Q_\nu}\,\frac{M_g}{M_d}\,.$$

In our case C has a value of 50 kg m^{-2} which is probably good to a factor of 2 (such a factor will add or subtract 2 K to the temperatures). A gas-to-dust ratio of 200 was assumed (see § V*b*). Figure 6*d* shows the results of the calculations. The mean temperature is 29 K (1 $\sigma = 4.4$ K), 5 K smaller than $\langle T_d(60/100)\rangle$. The temperatures are the lowest in the molecular cloud cores (24 K and 21 K in the northeastern and southwestern components, respectively). The temperatures located on the side of the molecular cloud facing the H II region have values very close to $T_d(60/100)$ showing that this periphery of the molecular cloud contains warm grains. Of course the information given by this procedure is limited. If very cold grains are present in the S142 molecular cloud their emission is too small to be detected in the 100 μm band. However we feel that the exciting stars have a strong impact on the NE component of the molecular cloud. The UV photons may penetrate in the molecular material via the intercondensation medium (see § III*bii*) and heat part of the embedded dust. Observations by Chini *et al.* (1986*a*, *b*) of heavily obscured compact H II regions at 1.3 mm give $T_d(100/1300) = 26$ K for the surrounding dust cloud giving credence to our hypothesis. The majority of these H II regions are excited by O-type stars. We therefore believe that the amount of very cold dust is limited in the S142 gas complex, the highest proportion being located in the SW component of the molecular cloud which contributes little to the 100 μm emission (see Fig. 11*a*).

The dust temperature derived from the 12 and 25 μm bands is relatively high, reaching temperatures of more than 200 K. Moreover the intensity at those wavelengths are higher than the intensity expected from interstellar grains in thermal equilibrium. This indicates the presence of different heating mechanisms for hot and warm grains. Recently many workers (Sellgren, Werner, and Dinerstein 1983; Leger and Puget 1984; Allamandola, Tielens, and Barker 1985) have suggested that the near-IR emission emitted by nebulae comes from very small grains (VSG) having sizes of the order of 5 Å. Those sturdy graphite molecules, composed of ~50 carbon atoms, are transiently heated by absorbing a single UV photon. These thermally fluctuating grains have been the subject of many studies (see Omont 1986 and references therein).

The *IRAS* observations were not specifically tailored for the study of VSGs. However the near-IR data tend to confirm their presence. Exploiting part of the results presented here we can derive the abundance of VSGs. First we compare the near- and far-IR emission (Leger and d'Hendecourt 1986) to derive their relative abundance with respect to large dust grains:

$$\frac{F_{12\,\mu{\rm m}}}{F_{100\,\mu{\rm m}}} = \frac{\sigma_{\rm vsg}{}^{\rm uv}N_{\rm vsg}}{\sigma_d{}^{\rm uv}N_d}\,,$$

where $\sigma_i{}^{\rm uv}$ is the UV cross section, N_i is the abundance, and F_i is the intensity at the appropriate wavelength. The UV cross section is given by $2\pi a^2$ for large grains ($a = 0.1$ μm), and by $5 \times 10^{-18} n_c$ (n_c is the number of carbon atoms) for the VSGs (Omont 1986). The intensity ratio was calculated to be 0.03. If the VSGs have 50 carbon atoms then we have $N_{\rm vsg} = 7.6 \times 10^4 N_d$. VSGs are much more abundant than dust grains but represent only a fraction of the mass. Using a gas-to-dust ratio of 200 (see § V*b*) we get VSG/H $= 4 \times 10^{-8}$. Assuming a carbon abundance C/H $= 4 \times 10^{-4}$ we get that 0.5% of carbon atoms are locked up in VSGs, 6 times less than what was derived for a reflection nebulae by Leger and Puget (1984). This is in agreement with the model of Puget, Leger, and Boulanger (1985) where the contribution of the VSGs to the emission decreases with increasing exciting star spectral type, the VSGs being more subject to evaporation. We mentioned earlier that $T_d(12/25)$ is the highest in the northeastern section of the complex. This section is the locus of all three gas phases and is far from the exciting star. When VSGs are concerned, a temperature increase indicates an increase in the amount of very small grains (F. X. Desert, private communication). Indeed $T_d(12/25)$ is the lowest near the main exciting star (see Fig. 6*a*), where the amount of VSGs is minimal due to their evaporation by the strong UV flux.

The optical depth (τ) was calculated at each wavelength using the relation found in Evans (1980),

$$\tau_\lambda = \frac{I_\nu(\lambda)\lambda^3}{2hc}\,\frac{e^{(h\nu)/kT_D} - 1}{\Omega}$$

which assumes that the emission uniformly fills the beam. Figures 7(*a*–*d*) present the variations of τ and consequently of the amount of dust grains across the gas complex at each wavelength. $T_d(12/25)$ was used to calculate τ_{12} and τ_{25}; $T_d(60/100)$ was used for τ_{60} and τ_{100}. The values have an uncertainty of 50%. The quantities τ_{12} and τ_{25} have their maximum value located between the two ionizing stars away from the peaks of emission and the peak temperature. The amount of hot dust falls off rapidly away from the maximum value. Since $\tau \approx N_d a^3$, where N_d is the dust column density and a is the grain radius, the variations of τ could instead be explained by variations in the grain radius. Local variations of a are probable, but we feel that a systematic decrease is difficult to justify physically. In any one direction the rate of decrease varies. However if we cut the gas complex in concentric annuli centered on the maximum value of τ and calculate the mean value of every optical depth point having the same radius, we obtain a power-law decrease of the amount of hot dust grains. Figure 8*a* shows the relation between the optical depth at 12 and 25 μm and the radius. The τ_{12} behavior is difficult to interpret since it should not have any meaning when one deals with

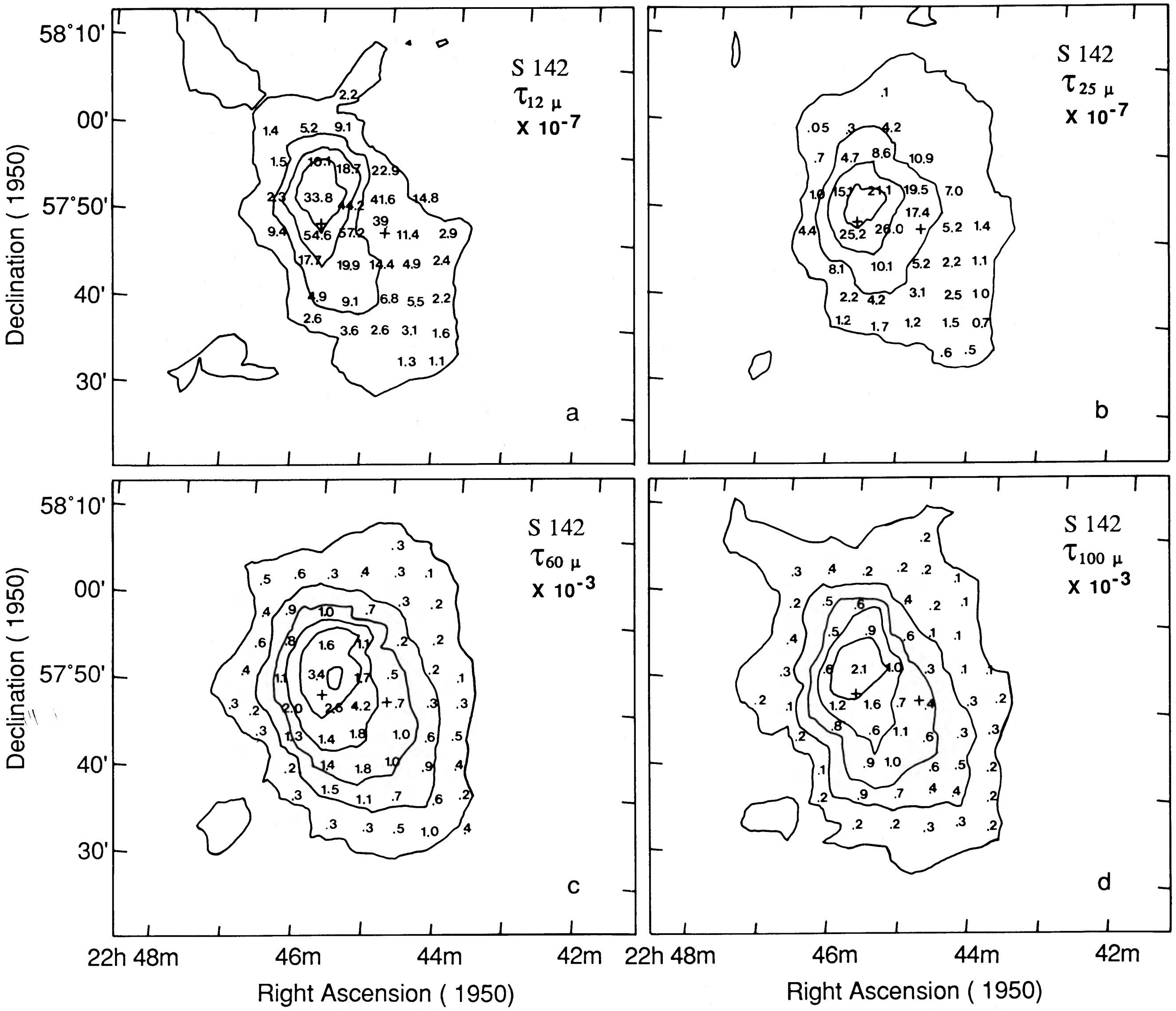

FIG. 7*a–d*.—The calculated optical depths (12, 25, 60, and 100 μm) are superposed to the appropriate contour maps (12, 25, 60, and 100 μm). The data were binned to give a 4′ spatial resolution. The crosses have the same function as in Fig. 5.

VSGs. We believe there is a contribution from the larger hot dust grains to the flux at less than 25 μm. These results indicate that part of the emission at 12 and 25 μm comes from the same hot dust grains, that the hot dust is inside the H II region (from the similarity of the continuum emission at 12 μm, 25 μm, and 21 cm), and that there is a larger quantity of hot dust where the radiation field is at its highest. The highest values of τ_{60} and τ_{100} coincide with their respective emission peak. Like the optical depth at 12 and 25 μm, τ_{60} and τ_{100} decrease from their peak value to the outskirt of the gas complex following a power law albeit with a higher exponent. Figure 8*b* shows this relation and the behavior of the 100 μm intensity with radius. The resemblance is striking and indicates that Figure 8*b* is an accurate representation of the distribution of the dust column density. This information is related to colder grains probably located in the outer sections of the H II region and the interface with the molecular cloud. At every wavelength the peak dust temperature is offset from the peak optical depth; the cloud is thus externally heated.

The following relation (Hildebrand 1983) was used to calculate the mass of dust (M_d)

$$M_d = \frac{4a\rho}{3Q_\nu}\frac{F_\nu D^2}{B_{(\nu,T)}}\,,$$

where a is the grain radius which we assume to be 0.1 μm, ρ is the gain density, Q_ν is the absorption efficiency, D is the distance to the gas complex, F_ν is the flux density, and $B_{(\nu,T)}$ is the Planck function for dust temperature T [where T was taken to be $T_d(12/25)$ or $T_d(60/100)$]. Since emission from graphite grains dominates the flux density at wavelengths smaller than 200 μm, we use a value of 2.25 gr/cm^3 for the grain density. The emissivity values were taken from an updated version (1987) of the computations of Draine (1985). The use of this equation implies that the grains are spherical and of uniform size, composition, and temperature. The mass of dust radiating at 12 and 100 μm is respectively $2.4 \pm 0.6 \times 10^{-1}\ M_\odot$ (a value of $a = 0.01\ \mu$m was used in this case) and $58 \pm 12\ M_\odot$.

The total IR flux density at each wavelength was found by

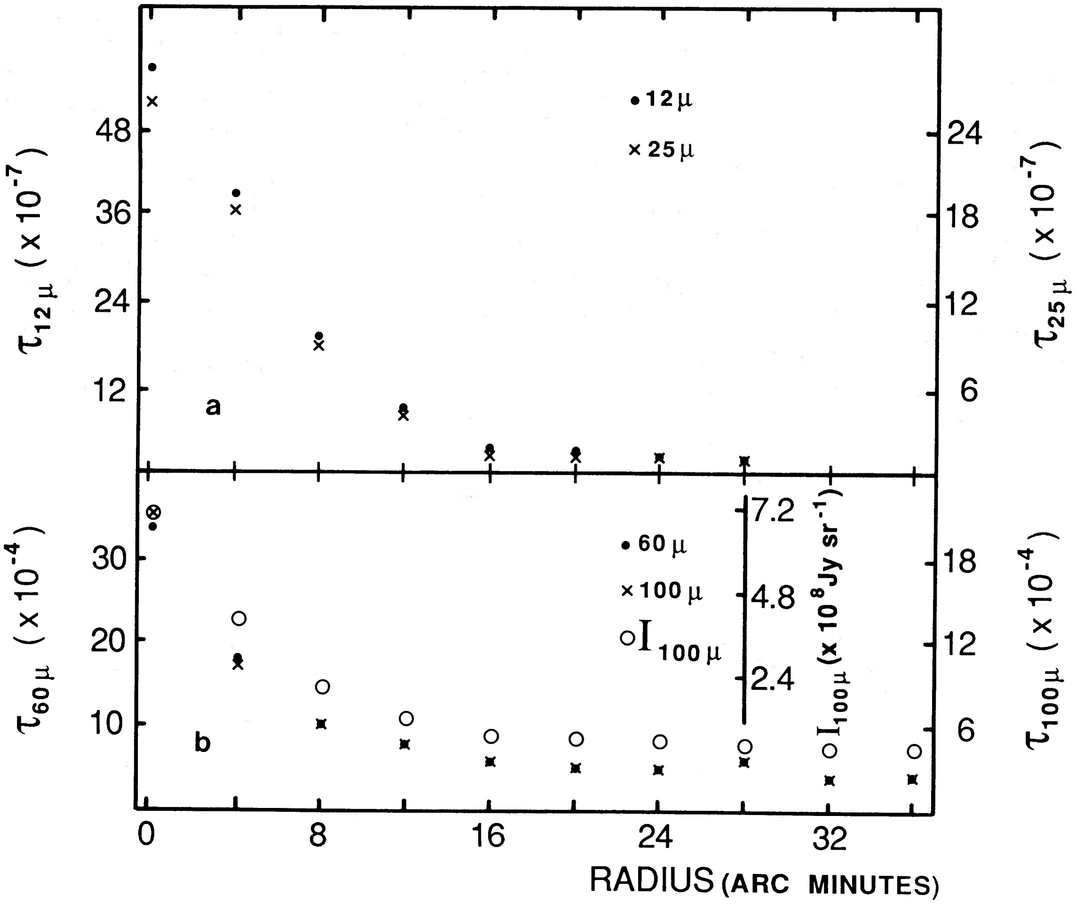

FIG. 8.—(*a*) Radial profile (see text) of the 12 and 25 μm optical depths. The apex is at the position of the maximum value as shown in Fig. 7*a*–*b*. (*b*) Radial profile of the 60 and 100 μm optical depths and the 100 μm intensity. The apex is at the position of their respective maximum value as shown in Fig. 7*c*–*d*.

integrating the contour maps in Figure 5. The results are listed in Table 4. From these the total IR flux can be derived: $F_{\rm IR} = 8.5 \pm 0.8 \times 10^{-10}$ J s^{-1} m^{-2}. The radiation falling outside the *IRAS* bands has been accounted for using a υB_υ spectrum spanning from 8 to 2200 μm. Using the total stellar flux from the main exciting star HD 215835 (O6+O6), we can derive some information concerning the geometry of the gas complex. From Panagia (1973), we have $F_* = 1.9 \times 10^{-9}$ J s^{-1} m^{-2} giving $F_{\rm ir}/F_* = 0.44$. If we assume that all the emitted stellar flux is eventually transformed into infrared radiation (of course this is not strictly true since part of the $\lambda > 912$ Å photons are not absorbed by the dust; however we do not take into account the presence of the O9 star thus its radiation partly fills in for the escaping photons), then this gas complex subtends a solid angle of 5.5 sr (44% of a 4π sr sphere) as seen from the star. Using the area of the 2 σ contour of the 100 μm emission, we get consistent solid angles if the cloud is tilted approximately 50° into the plane of the sky, i.e., with respect to the line of sight. This is in agreement with the model used in Paper II to derive the density distribution of the ionized gas.

The IR excess (see the appendix in Gatley *et al.* 1978 for a discussion on this parameter) for the S142 gas complex has a value of 7.5, indicating that part of the Lyman continuum (Ly$_c$) photons emitted by the stars are absorbed by the dust grain. To evaluate the dust optical depth (τ_1) for Ly$_c$ photons in the ionized region we use (Petrosian, Silk, and Field 1972; Hackwell *et al.* 1978)

$$L_{\rm IR} = L_\alpha + [1 - \exp(\tau_1)]L_c + [1 - \exp(\tau_2)]L_{\lambda > 912\,{\rm A}}\,,$$

where $L_{\rm IR}$ is the total IR luminosity of the object, L_α is the Lyman α photon luminosity, L_c is the Ly$_c$ photon luminosity emitted by the stars, τ_2 is the optical depth for the photons having a wavelength larger than 912 Å, and $L_{\lambda > 912\,{\rm Å}}$ is the photon luminosity emitted by the stars longward of the Lyman continuum. For the case under study, $L_{\rm IR} = 3.3 \pm 0.3 \times 10^5$ $L_\odot$, $L_\alpha = 1.6 \times 10^5$ $L_\odot$, $L_c = 3.5 \times 10^5$ $L_\odot$, and $L_{\lambda > 912\,{\rm Å}} = 4.5 \times 10^5$ $L_\odot$ (the star characteristics were taken from Panagia 1973). We thus get a relation between τ_1 and τ_2. If $\tau_2 = 0$, τ_1 has a maximum value of 0.7. If $\tau_1 = \tau_2$, the optical depth is 0.2. Since these two values are extremes, the fraction of Ly$_c$ photons absorbed by the dust is between 20% and 60%.

To check on the consistency of our model for the H II region (Paper II) we use this relation from Hackwell *et al.* (1978)

$$L_\alpha = \frac{h\nu_\alpha \beta N_e M}{m_{\rm H}}\,,$$

where β is the recombination coefficient being 5.0×10^{-13} cm^3 s^{-1}, M is the mass of the ionized gas, and N_e is the electron density (we calculated a mean value of 15 cm^{-3}). We thus get $M = 4120$ $M_\odot$, very close to the value derived from the radio observations (4000 $M_\odot$).

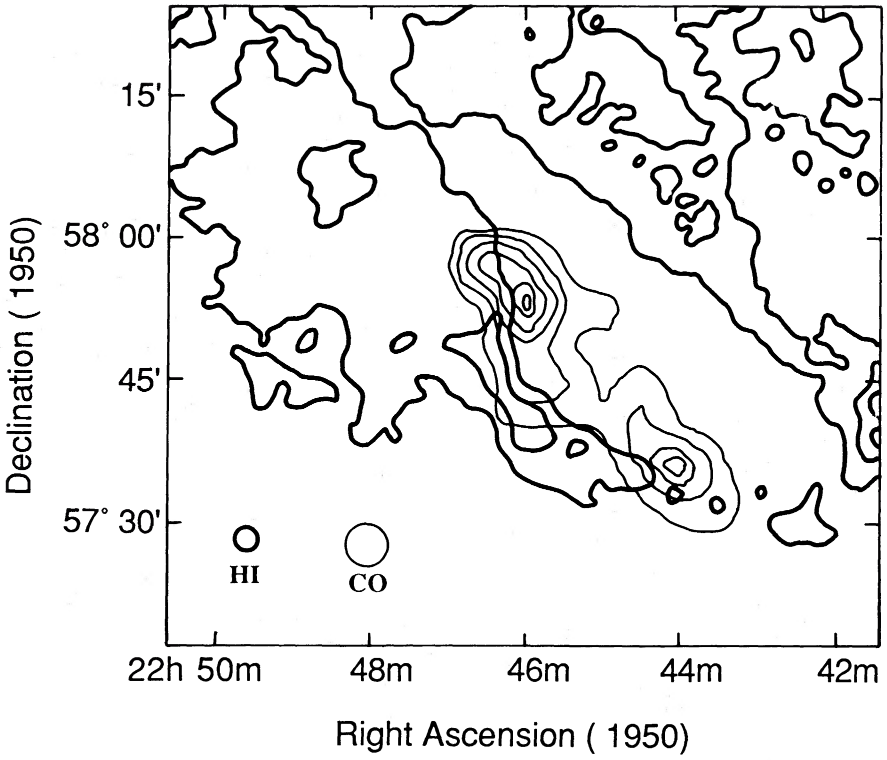

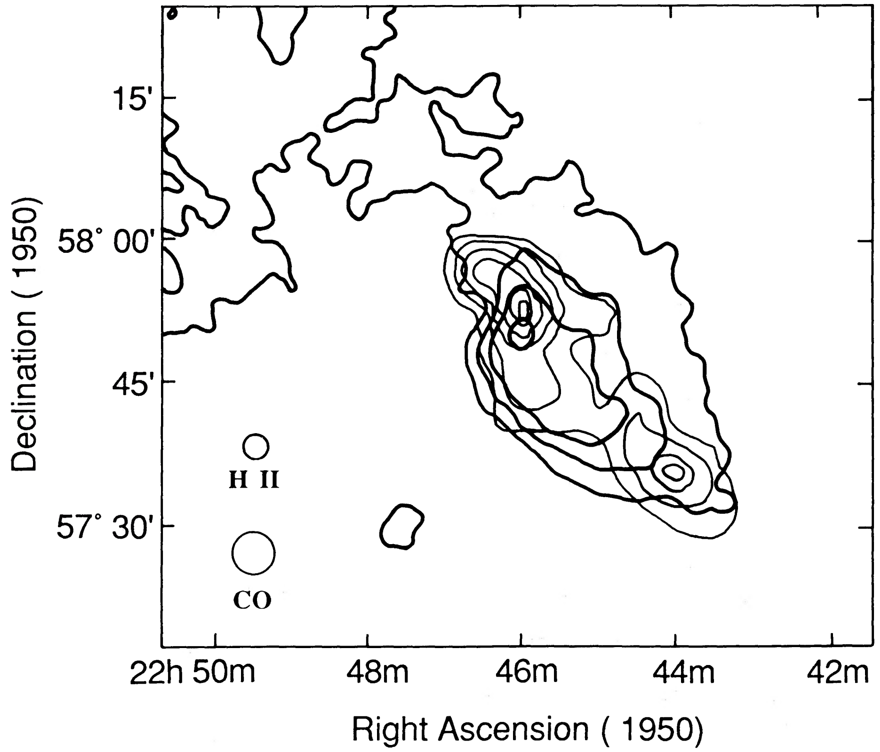

FIG. 9.—(*a*) A superposition of the ^{13}CO antenna temperature map (HPBW = 4.′4) on the H I average brightness map (−36.6 to −47.1 km s^{-1}) of feature B (HPBW = 2′). The lowest contour level of the ^{13}CO map is 0.24 K, the highest is 0.85 K. The contour interval for the H I map is 4 K. (*b*) A superposition of the ^{13}CO antenna temperature map on the radio continuum map. The characteristics of this figure are the same as Fig. 9*a*, except that the radio continuum map has a 2 K contour interval.

V. COMPARISON OF THE CO, H I, AND IR DATA

a) *Morphology*

Figures 9*a*–*b* show a superposition of the ^{13}CO and radio observations. An H I emission feature called feature B (see Paper II and Fig. 9*a*) is clearly related to S142. It was integrated over the velocity range -36.6 to -47.1 km s^{-1}, similar to the ^{13}CO velocity range. Feature B lies on the eastern side of the molecular cloud while the latter overlays the radio continuum emission (Fig. 9*b*); all three gas components follow the same orientation. This geometry is different from the one pictured in Figure 6 of Paper II where the CO map of Israel (1980) is depicted. We explain this discrepancy by the higher resolution and deeper survey of our observations. Feature B, which is likely dissociated molecular material, smoothly follows the velocity difference between the two components of the molecular cloud: the less negative velocities are in the southwestern part while the more negative velocities are in the northeastern part. The same is true for the Hα velocity field whose eastern edge follows the kinematic behavior of feature B (see Paper I). The molecular cloud is behind the H II region and probably closely behind and partly intertwined with feature B. This feature is probably located in the same "plane" as the ionized gas being overwhelmed by the UV photons (optically visible ionized gas is present in front of the feature). What we are probably seeing is a truncated cone whose left side is mostly H I gas (feature B) and whose far side is molecular gas. The reason why we do not detect any H I in front of the molecular gas may be explained simply by its paucity because of the particular location of the ionizing stars. Figure 10 depicts our interpretation of the position and interaction of the various components of the S142 gas complex.

Figure 11*a* is a superposition of the ^{13}CO and 100 μm emission. The 100 μm peak intensity coincides with the NE core of the molecular cloud. The SW core does not show any IR enhancement; in addition the IR emission does not cover completely this section of the cloud. This may be caused by the presence of colder grains (see § IV*b*) emitting longward of 100 μm and implying a shortage of heating radiation in agreement with the lack of H I. Everywhere else the 100 μm emission is more extensive than the ^{13}CO and ^{12}CO emission. In fact the 100 μm emission resembles more the 21 cm continuum emission from the H II than the molecular cloud. We tried to find a relation between the integrated ^{12}CO emission and the IR intensity at 100 μm. No clear relation was found, $\int {}^{12}\mathrm{CO}\, dV = (0.004\text{–}0.2) I_{100}$. The warm dust emission may thus come from the H II region and the outer layers of the molecular cloud facing the exciting stars. Dust grains may also be present in feature B (there is an extension of the IR emission on the eastern side following the H I contours, see Fig. 11*b*) and the outskirt of the H II region. The northern spikes present in the 3 σ contour may be explained by the presence of a lot of H I connected to features B and C (see Figs. 3 and 4 of Paper II) and possibly heated by the ionizing stars or the interstellar radiation field.

b) *Linked Properties*

i) *The Gas-to-Dust Ratio*

Let us sum up the masses of the different gas components (assuming optically thin conditions and no clumping):

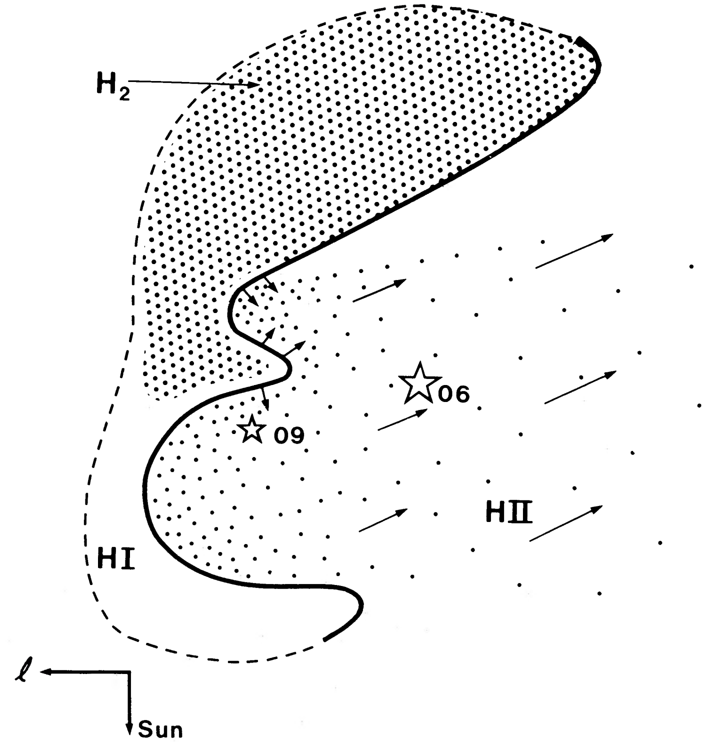

FIG. 10.—A schematic representation of the S142 star and gas complex. The various gas components are shown as well as the principal ionizing stars. The molecular cloud extends behind and away from the ionized gas. The cold dust grains are in the molecular cloud. The H I forms a shell between the molecular and ionized material. The ionized gas is flowing away from the neutral gas at large speeds and is the densest close to the neutral material. The hot and warm dust grains are inside the H II region.

1988ApJ...332.1030J

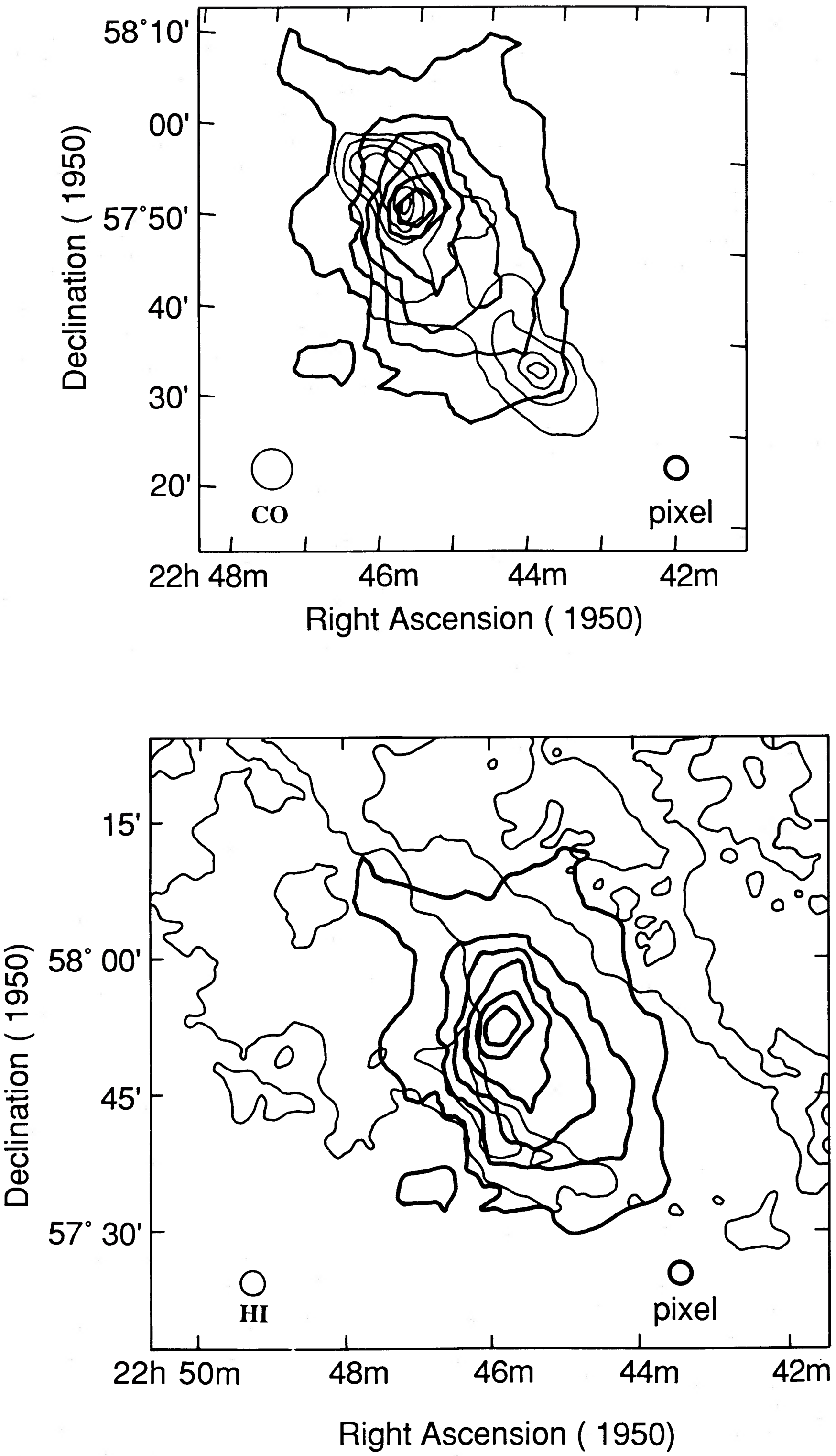

FIG. 11*a*.—A superposition of the ^{13}CO antenna temperature map on the 100 μm map. The ^{13}CO map is the same as in Fig. 9. The 100 μm contours are at 105.5, 164.9, 257.6, 402.5, 628.9, and 786.2 M Jy sr^{-1}. (*b*) A superposition of the 100 μm map with the H I emission feature B. The map characteristics are the same as in Figs. 9*a* and 11*a*.

H II region	4000 $M_\odot$
Feature B (H I)	1200 $M_\odot$
Feature C (H I)	1800 $M_\odot$
H_2 region	5600 $M_\odot$
Warm dust	60 $M_\odot$
Hot dust	0.24 $M_\odot$

For the mass of the molecular cloud we used the mean value of the calculated lower and upper limit (§ III*a*ii). Taking into account all components we obtain a gas-to-dust ratio of ~200, consistent with the fact that the S142 gas complex is an evolved object. However one must keep in mind the large uncertainties in the mass estimates and the fact that the amount of cold dust present in the depth of the molecular cloud is undetermined.

ii) *The Star Formation Efficiency*

The next step is to evaluate the total mass of the star cluster NGC 7380 by computing its initial mass function (IMF). Our goal is to determine the star formation efficiency in the S142 complex. Following the usual procedure as described in Yamanaka (1987) we used a power-law function for the IMF [$\Phi(m)$]:

$$\Phi_{(m)} = Am^{-(1+x)} ,$$

where m is the star mass and A is a constant chosen so that

$$\int_{m_{\rm lower}}^{m_{\rm upper}} m\Phi_{(m)}\, dm = 1.0 .$$

The exponent x was determined using the information given in Moffat (1971) and Baade (1983) about the star cluster: NGC 7380 contains 192 stars with $m_v \leq 17$ mag (i.e., with $m \geq 1$ $M_\odot$), two O6V stars (giving $m_{\rm upper} = 40$ $M_\odot$) and given numbers of different O-type stars. Their masses were determined using the relations found in Humphreys and McElroy (1984). A value of 0.1 $M_\odot$ was chosen for $m_{\rm lower}$. The relation

$$n_i = \int_{m_-}^{m_+} \Phi_{(m)}\, dm ,$$

$$m_- = \sqrt{m_{i-1} m_i} , \quad m_+ = \sqrt{m_i m_{i+1}}$$

was used to compute the number of stars at each mass m in the mass interval m to $m + dm$. A value of $x = 0.89$ best satisfies the abovementioned conditions, giving a total mass of ~1000 $M_\odot$ for the star cluster. NGC 7380 seems to have a lower number of high-mass stars than produced analytically. Since the spectroscopic observations of the star cluster are not complete these stars may have been missed. This value of the total mass is possibly accurate to within 50%; the star cluster mass cannot be less than ~500 $M_\odot$.

The star formation efficiency is defined as the ratio of the cluster mass and the total mass of the complex (gas + stars). We obtain a value of 0.08, smaller than what is derived theoretically (0.22 to 0.59) by Elmegreen (1983), Mathieu (1983), and Rengarajan (1984). The highest efficiency we can get by taking into account generous uncertainties in the mass estimates is 17%. NGC 7380 is an old cluster (2–3 × 10^6 yr) and the molecular cloud is disrupted; we can thus suppose that the formation of massive stars, and possibly of low mass stars, is over. Thus we do not anticipate any change of our calculated efficiency with time. Considering the uncertainties of our mass estimates we can only state that our result is close to the lower end of the theoretical values and that star formation in S142 may not have been very efficient. There are very few gas complexes that have been as extensively studied as S142. More work is needed before the observations can really sanction the theory.

Extragalactic CO astronomers use a different way to measure the star formation efficiency: the ratio of the far-IR luminosity to the CO luminosity (Solomon *et al.* 1987). For the S142 gas complex, log $L_{\rm FIR}$ ($L_\odot$) = 4.9 and log $L_{\rm CO}$ (K km s^{-1} pc^2) = 3.3. Compared with other gas complexes S142 is overluminous in the far-IR or underluminous in CO. This may come from the fact that S142 is an old object.

iii) *Energetics of the Molecular Gas Cloud*

Molecular clouds are mostly cooled by line emission from various molecules (under certain conditions dust grains can contribute). Under normal cloud conditions (away from ionizing radiation) ^{12}CO is the main contributor. Extensive theoretical calculations have been carried out by Goldsmith and Langer (1978) where they derive the ^{12}CO cooling rate to be ($n_{\rm H_2} = 10^3$ cm^{-3}, 10 K $\leq T_K \leq$ 60 K)

$$\Lambda = 6.8 \times 10^{-22} T_K{}^{2.2} \text{ ergs cm}^{-3}\text{ s}^{-1} .$$

We have already discussed in § III*a* that the S142 molecular cloud is composed of two components. For the purpose of our calculations we separate each component into a core and an outer region; we assume spherical symmetry. The mean kinetic temperature (T_K) and the volume of each region are shown in Table 6. We assume throughout that $n_{\rm H_2} \approx 10^3$ cm^{-3}. Although the previous relation only applies in a limited temperature range, we assume it still holds for $T_K \approx 5$ K. The calculations are displayed in Table 6.

Let us now consider the heating sources. The S142 molecular cloud does not contain any strong IR sources which could contribute to the cloud heating. We discard also heating by gravitational contraction and ambipolar diffusion, which depends on gravitational contraction, since they appear to play a role only in clouds with densities higher than any density estimation of the S142 molecular cloud (this study and Ungerechts, Walmsley, and Winnewisser [1982] did not detect any NH$_3$ emission from S142). In addition the velocity field of the molecular cloud does not show the presence of either contraction or expansion. Another possible mechanism is heating by dust grains. The relation giving the rate of energy transfer between dust and gas is given by Goldsmith and Langer (1978). However they argue that molecular hydrogen densities greater than or equal to 10^5 cm^{-3} are required to closely couple the dust and gas temperatures in warm clouds. If such is the case in the core of the S142 molecular cloud ($T_K \approx 10$ K), the cold dust grains ($T < 20$ K) should not contribute much to the heating. In the outer layers of the molecular cloud where the dust is warmer an exchange of energy is possible but our observations do not permit us to quantify it.

The only known heating mechanism left is heating by cosmic rays. Goldsmith and Langer give for the heating rate

$$\Gamma = 6.4 \times 10^{-28} n_{\rm H_2} \text{ ergs cm}^{-3}\text{ s}^{-1}$$

TABLE 6

THERMAL BALANCE CALCULATIONS

Region	Volume cm^3	T_K K	Λ $L_\odot$	Γ $L_\odot$
Core NE	9.6 × 10^{56}	8.0	0.17	0.16
Outer NE	1.9 × 10^{58}	4.5	0.92	3.2
Core SW	1.5 × 10^{57}	8.0	0.26	0.25
Outer SW	1.6 × 10^{58}	4.8	0.90	2.7

The results are shown in Table 6. The heating and cooling rates are almost equal in the core regions, but the heating rates are too large by a factor of 3 in the outer regions. This discrepancy can be explained by the special nature of cloud edges (the periphery of the molecular cloud facing the exciting stars) where ion cooling rates must be taken into account and where the presence of hot dust can still be a factor. Our lack of a systematic high spatial resolution mapping may also be a factor in explaining the discrepancy.

VI. SUMMARY

We have presented results of millimeter and infrared wavelength observations of the S142 gas complex. Our main conclusions from millimeter line observations of the molecular cloud are the following.

1. It is much larger and much more massive than previous observations had revealed. The molecular cloud has an extent of roughly 30 pc and a mass of $\sim 5600\ M_{\odot}$. It is also made up of large density condensations.
2. It contains two cores separated spatially by 25 projected parsecs and kinematically by 4 km s^{-1}.
3. Its orientation is the same as an H I feature having the same LSR velocity as the H II region.
4. Although it is made up of higher density condensations the molecular cloud seems, at least in part, disrupted by the UV photons from the exciting stars.

The IRAS observations reveal:

1. The presence of a possible T Tauri star indicating that star formation in S142 spanned a relatively long time interval (0.5–1.0×10^6 yr);
2. that the near-IR emission is coextensive with and follows closely the features of the ionized gas, while the far-IR emission resembles more the contours of the H II region than those of the molecular cloud;
3. that part of the near-IR emission comes from very small grains while the mid- and far-IR emission is from large grains. The quantity of very small grains is the highest where the radiation field is the most tenuous. The southwestern core of the molecular cloud has little IR emission indicating that it is less affected by the UV photons;
4. the amount of emitting dust falls off rapidly away from its peak position. There is a relatively small amount of warm dust ($\sim 60\ M_{\odot}$) in S142.

Our overall picture of the S142 gas complex does not change much from the one shown in Paper II (compare Fig. 9 of Paper II to Fig. 10 presented here). The only difference is that the molecular gas is behind the H II region rather than coplanar with it. There is little CO gas east of feature B and probably only a small fraction inside it. S142 is like a truncated cone seen inclined $\sim 50°$ with respect to the observer. The far face is molecular gas, the truncated part is H I gas, while the near face is mostly ionized gas with some H I (feature C). The warm dust grains are mostly located in the outskirts of the H II region and the outer part of the molecular cloud facing the exciting star. The presence of a spatially and kinematically different southwesterly core in the molecular cloud is a little puzzling. The velocity difference is too small to make them distinct clouds. Moreover feature B is smoothly connected in velocity to both cores. This brings us to suggest that star formation in the S142 area may have been triggered by the collision of two nearby molecular clouds. This is possible since high-mass star formation cannot take place in dense clouds without some external force (Turner 1984; Scoville, Sanders, and Clemens 1986). We derived a star formation efficiency of $\sim 8\%$ for this complex.

We thank the C.N.R.S. (A.T.P.P.C.M.I.) and the Institut National des Sciences de l'Univers for their financial support of the Bordeaux radiotelescope. One of us (G. J.) would like to thank V. A. Hughes for his hospitality at Queen's University where part of this work was done and J. Yamanaka for the use of her IMF program. G. J. is also happy to acknowledge the National Science and Engineering Research Council of Canada for its support. We are grateful to A. Baudry from the Observatoire de Bordeaux for taking the Pico Veleta observations and M. Andersson for his help during the Onsala observations.

REFERENCES

Allamandola, L. J., Tielens, A. G. G. M., and Barker, J. R. 1985, *Ap. J.* (*Letters*), **290**, L25.

Baade, D. 1983, *Astr. Ap. Suppl.*, **51**, 235.

Baudry, A., Cernicharo, J., Pérault, M., de La Noë, J., and Despois, D. 1981, *Astr. Ap.*, **104**, 101.

Beichman, C. A., Myers, P. C., Emerson, J. P., Harris, S., Mathieu, R., Benson, P. J., and Jennings, R. E. 1986, *Ap. J.*, **307**, 337.

Blitz, L., and Stark, A. A. 1986, *Ap. J.* (*Letters*), **300**, L89.

Bloemen, J. B. G. M., Strong, A. W., Blitz, L., Cohen, R. S., Dame, T. M., Grabelsky, D. A., Hermsen, W., Lebrun, F., Mayer-Hasselwander, H. A., and Thaddeus, P. 1986, *Astr. Ap.*, **154**, 25.

Bohlin, R. C., Savage, B. D., and Drake, J. F. 1978, *Ap. J.*, **224**, 132.

Chini, R., Kreysa, E., Mezger, P. G., and Gemünd, H.-P. 1986*a*, *Astr. Ap.*, **154**, L8.

———. 1986*b*, *Astr. Ap.*, **157**, L1.

Dickman, R. L. 1978*a*, *Ap. J. Suppl.*, **37**, 407.

———. 1978*b*, *A.J.*, **83**, 363.

Draine, B. T. 1985, *Ap. J. Suppl.*, **57**, 587.

Elmegreen, B. G. 1983, *M.N.R.A.S.*, **203**, 1011.

Evans, N. J., II. 1980, in *IAU Symposium 87, Interstellar Molecules*, ed. B. Andrew (Dordrecht: Reidel), p. 1.

Gatley, I., Becklin, E. E., Werner, M. W., and Harper, D. A. 1978, *Ap. J.*, **220**, 822.

Goldsmith, P. F., and Langer, W. D. 1978, *Ap. J.*, **222**, 881.

Hackwell, J. A., Gehrz, R. D., Smith, J. R., and Briotta, D. A. 1978, *Ap. J.*, **221**, 797.

Hildebrand, R. D. 1983, *Quart. J.R.A.S.*, **24**, 267.

Humphreys, R. M., and McElroy, D. B. 1984, *Ap. J.*, **284**, 565.

Infrared Astronomical Satellite Catalogs and Atlases, Explanatory Supplement 1985, ed. C. A. Beichman, G. Neugebauer, H. J. Habing, P. E. Clegg, and T. J. Chester (Washington D.C.: U.S. Government Printing Office).

Israel, F. P. 1980, *A.J.*, **85**, 1612.

Joncas, G., Dewdney, P. E., Higgs, L. A., and Roy, J. R. 1985, *Ap. J.*, **298**, 596 (Paper II).

Joncas, G., and Roy, J. R. 1984, *Ap. J.*, **283**, 640 (Paper I).

Kahane, C., Guilloteau, S., and Lucas, R. 1985, *Astr. Ap.*, **146**, 325.

Kutner, M. L., and Ulich, B. L. 1981, *Ap. J.*, **250**, 341.

Leger, A., and d'Hendecourt, L. 1986, preprint, Les Houches Workshop, PAH's and Astrophysics.

Léger, A., and Puget, J. L. 1984, *Astr. Ap.*, **137**, L5.

Martin-Pintado, J., Wilson, T. L., Johnston, K. J., and Henkel, C. 1985, *Ap. J.*, **299**, 386.

Mathieu, R. D. 1983, *Ap. J.* (*Letters*), **267**, L97.

McKee, C. F., and Hollenbach, D. J. 1980, *Ann. Rev. Astr. Ap.*, **18**, 219.

Moffat, A. F. J. 1971, *Astr. Ap.*, **13**, 30.

Omont, A. 1986, *Astr. Ap.*, **164**, 159.

Panagia, N. 1973, *A.J.*, **78**, 929.

Pérault, M., Falgarone, E., and Puget, J. L. 1985, *Astr. Ap.*, **152**, 371.

Petrosian, V., Silk, J., and Field, G. B. 1972, *Ap. J.* (*Letters*), **177**, L69.

Puget, J. L., Léger, A., and Boulanger, F. 1985, *Astr. Ap.*, **142**, L19.

Rengarajan, T. N. 1984, *Ap. J.*, **287**, 671.

Scoville, N. Z., and Kwan, J. 1976, *Ap. J.*, **206**, 718.

Scoville, N. Z., Sanders, D. B., and Clemens, D. P. 1986, *Ap. J.* (*Letters*), **310**, L77.

Sellgren, K., Werner, M. W., and Dinerstein, H. L. 1983, *Ap. J.* (*Letters*), **271**, L13.
Solomon, P. M., Rivolo, A. R., Mooney, T. J., Barrett, J. W., and Sage, L. J. 1987, in *Star Formation in Galaxies*, ed. C. J. Lonsdale Persson (Washington: NASA), p. 37.
Turner, B. E. 1984, *Vistas Astr.*, **27**, 303.
Ungerechts, H., Walmsley, C. M., and Winnewisser, G. 1982, *Astr. Ap.*, **111**, 339.
Yamanaka, J. M. 1987, unpublished Ph.D. dissertation, Yale University.

GILLES JONCAS: Département de physique, Université Laval, Québec, Québec, G1K 7P4, Canada

CARSTEN KÖMPE and JÉROME DE LA NOË: Observatoire de l'Université de Bordeaux 1, Boîte Postale 21, F-33270 Floirac, France